Journal of Mathematical Modeling
Vol. 10, No. 3, 2022, pp. 467-486. Research Article

JMM

An iterative variational model for blind image deconvolution

Bouchra Laaziri*, Abdelilah Hakim, Said Raghay

Department of Mathematics, University of Cadi Ayyad, Marrakesh, Morocco
Email(s): bouchra.laaziri@ced.uca.ac.ma, a.hakim@uca.ma, s.raghay@uca.ma

Abstract. Classical image deconvolution seeks an estimate of the true image when the blur kernel or the point spread function (PSF) of the blurring system is known a priori. However, blind image deconvolution addresses the much more complicated, but realistic problem where the PSF is unknown. Bayesian inference approach with appropriate priors on the image and the blur has been used successfully to solve this blind problem, in particular with a Gaussian prior and a joint maximum a posteriori (JMAP) estimation. However, this technique is unstable and suffers from significant ringing artifacts in various applications. To overcome these limitations, we propose a regularized version using H^1 regularization terms on both the sharp image and the blur kernel. We present also useful techniques for estimating the smoothing parameters. We were able to derive an efficient algorithm that produces high quality deblurred results compared to some well-known methods in the literature.

Keywords: Blind image deconvolution, supervised Bayesian approach, regularization.
AMS Subject Classification 2010: 94A08, 62F15, 47A52.

1 Introduction

Over the last few years, image deconvolution has attracted increasing attention, considering the major function of image restoration in advanced imaging systems to provide high-quality images under complex environments such as motion, inappropriate lighting settings, and inaccurate device components. It is a classical inverse problem that aims to restore a sharp image from the degraded (blurry and/or noisy) version. For several applications for image processing, this recovery process is important. Even though classical linear image deconvolution has been studied extensively [1, 15, 19], the more difficult problem of blind image deconvolution has numerous possibilities for study. It is the procedure of estimating the true image $f(x,y)$ as well as the blur kernel $h(x,y)$ from the degraded image $g(x,y)$ characteristics, using partial image information. Mathematically, this problem can be formulated as the linear spatially invariant (LSI) system

$$g(x,y) = h(x,y) * f(x,y) + \varepsilon(x,y), \tag{1}$$

*Corresponding author.
Received: 7 December 2021 / Revised: 21 January 2022/ Accepted: 18 February 2022
DOI: 10.22124/jmm.2022.21262.1862

where $*$ represents the convolution operation and $\varepsilon(x,y)$ the errors (modeling, linearization, and the other unmodeled errors often called noise).

In many applications including astronomical speckle imaging [4], remote sensing [22], and medical imaging [8, 10, 16, 29], deconvolution is performed for image restoration. Generally, the PSF $h(x,y)$ is assumed to be specifically defined before the deconvolution process, and the problem of restoring the sharp image is known as the traditional linear non-blind image deconvolution problem. In this case, there are a variety of well-known techniques in the long list of deconvolution methods, such as inverse filtering, Wiener filtering, least-squares (LS) filtering, recursive Kalman filtering, and constrained iterative deconvolution methods [5, 14, 15].

Unfortunately, the blur is often unknown in many realistic cases, and little information about the true image is available. By using partial or no knowledge of the blurring process and the true image, the original image $f(x,y)$ should then be determined directly from $g(x,y)$. Such a problem refers to finding estimates $\tilde{f}$ and $\tilde{h}$ for f and h based on g and prior knowledge about f, h, and ε, assuming the linear degradation model (1).

For image processing applications, there are different motivating facts behind the use of blind deconvolution. In reality, having a priori data about the imaged scene is often expensive, risky, or physically impractical. For example, it is hard to statistically model the original image in applications such as remote sensing and astronomy, or even know specific details about scenes that have never been imaged before [4, 22]. Furthermore, the degradation due to blurring can not be defined precisely. In aerial imaging and astronomy, the blurring can not be properly modeled as a random process since PSF fluctuations are difficult to characterize [27]. In real-time image processing, such as medical video-conferencing, it is not possible to predetermine the PSF parameters to directly deblur images [7]. In addition, online identification techniques used to estimate degradation can lead to substantial errors that can produce artifacts in the restored image [25].

The physical necessities for enhanced image quality are unrealizable in other applications. For example, the physical weight of a high-resolution camera in space exploration might exceed practical constraints. Similarly, enhanced image quality occurs in x-ray imaging with increased incidental x-ray beam strength, which is harmful to the health of a patient [10]. Therefore, blurring is possible. The hardware available to measure the imaging system's PSF is often hard to use in such circumstances. Though these methods work well to determine the PSF, they are esoteric, restricting their widespread use [16,27]. Blind image deconvolution is a feasible option for enhancing the image quality without the need for complex methods of calibration.

Finally, adaptive-optics devices can be used to compensate for blurring degradations for applications such as astronomy, but the high cost of these systems makes the imaging impractical for certain observational facilities. The use of cheaper, partially compensating systems can result in phase errors. Post-processing, such as blind deconvolution, is needed in either situation to improve image quality [24, 26].

It is obviously clear that an algorithmic approach is required to combine sharp image recovery and blur kernel estimation. Blind deconvolution is in this sense a practical method for image restoration. Recent research in literature [3, 9, 12, 17, 18, 20, 27, 28] has in fact shown its value.

Blind image deconvolution is a highly ill-posed problem since there are infinite pairs of solutions. To get the ideal solution, some additional assumptions on f and h must be introduced, and by allowing both sharp image recovery and PSF identification to interact we can better avoid ringing artifacts and local minima.

Despite obtaining a certain level of development, blind deconvolution is limited in its success by

complicated application conditions, which make the blur difficult to achieve and be spatially variant. However, many novel practical approaches have been presented to handle this problem, driven by a variety of motivations.

The majority of existing methods fall into the class of joint identification methods, where the image and blur are identified simultaneously. However, in practice, many methods in this category use an alternating approach to estimate f and h rather than truly finding the joint solution.

In this article, we solve this blind problem. As both the sharp image f and the blur kernel h need to be updated at the same time, we use an iterative algorithm to optimize the parameters by applying an alternating minimization scheme.

The remaining of this paper is set out like the following. The second section reviews the supervised Bayesian approach. It exposes then the problem statement and explains the proposed model. A theoretical analysis revealing the existence of the solution to the problem has been presented. Section 3 addresses the experimental protocol and discusses the obtained results. Finally, a conclusion outlines the key points covered in the article.

2 Methods

In this section, we review the supervised Bayesian technique based on a Bayesian estimation using simple prior models to assign all the unknown parameters. Then, we extend this method by adding H^1 regularization terms on both the sharp image and the blur kernel, and by suggesting useful techniques to deal with the estimation of the smoothing parameters. Theoretically, we give a detailed description of the convergence behavior of our model, and we derive the proposed efficient alternating minimization algorithm.

2.1 Bayesian approach

From this point, the main objective is to infer on f and h given the forward model

$$g = Hf + \varepsilon, \tag{2}$$

where H represents the 2D convolution matrix obtained from the PSF of the imaging system [13]. This model is the discretized version of model (1), referring the reader to [21] for more details on this discretization.

In the reconstruction problems, we use the Bayes rule:

$$\begin{aligned} p(f,h|g) &= \frac{p(g|f,h)p(f)p(h)}{p(g)} \\ &\propto p(g|f,h)p(f)p(h), \end{aligned} \tag{3}$$

to obtain what is called the *posterior* law $p(f,h|g)$ from the likelihood $p(g|f,h)$ and the prior laws $p(f)$ and $p(h)$, and we can infer on f and h using this law.

2.1.1 Bayesian estimation with simple prior

As in blind deconvolution, both f and h are unknown, the Bayesian inference approach is based on the posterior law:

$$p(f,h|g,\theta_1,\theta_2,\theta_3) = \frac{p(g|f,h,\theta_1)p(f|\theta_2)p(h|\theta_3)}{p(g|\theta_1,\theta_2,\theta_3)} \propto p(g|f,h,\theta_1)p(f|\theta_2)p(h|\theta_3), \tag{4}$$

where the term $p(g|f,h,\theta_1)$ is the likelihood, $p(f|\theta_2)$, $p(h|\theta_3)$ are the prior models, $\theta = (\theta_1,\theta_2,\theta_3)$ contains their corresponding parameters (often called the hyper-parameters of the problem, e.g., the variances v_ε, v_f, and v_h of the noise ε, the true image f, and of the blur kernel h, respectively), and $p(g|\theta_1,\theta_2,\theta_3)$ is the evidence of the model. This is shown in the following scheme:

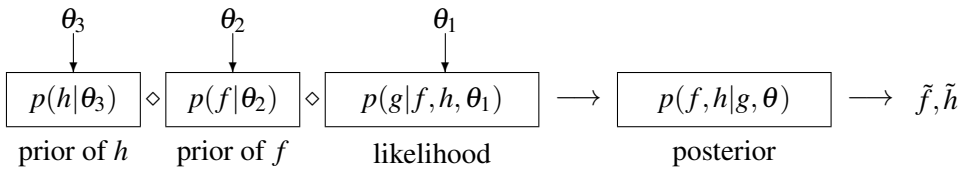

2.1.2 Supervised Bayesian approach

We consider ε, v_ε, v_f, and v_h are known, then the expression of the likelihood is:

$$p(g|f,h,v_\varepsilon) = \mathcal{N}(g|Hf, v_\varepsilon I). \tag{5}$$

The priors for f and h are:

$$p(f|v_f) = \mathcal{N}(f|0, v_f I), \tag{6}$$

and

$$p(h|v_h) = \mathcal{N}(h|0, v_h I). \tag{7}$$

The joint posterior of all the unknowns becomes:

$$p(f,h|g,v_\varepsilon,v_f,v_h) \propto p(g|f,h,v_\varepsilon)p(f|v_f)p(h|v_h). \tag{8}$$

We get the following estimates:

$$\begin{aligned}(\tilde{f},\tilde{h}) &= \arg\max_{(f,h)} \left\{p(f,h|g,v_\varepsilon,v_f,v_h)\right\} \\ &= \arg\max_{(f,h)} \left\{\exp\left(-\frac{1}{2v_\varepsilon}\|g-Hf\|_2^2\right)\exp\left(-\frac{1}{2v_f}\|f\|_2^2\right)\exp\left(-\frac{1}{2v_h}\|h\|_2^2\right)\right\} \\ &= \arg\min_{(f,h)} \left\{\frac{1}{2v_\varepsilon}\|g-Hf\|_2^2 + \frac{1}{2v_f}\|f\|_2^2 + \frac{1}{2v_h}\|h\|_2^2\right\}. \end{aligned} \tag{9}$$

Then, the functional to be minimized is

$$\begin{aligned}\mathfrak{J}(f,h) &= \frac{1}{2v_\varepsilon}\|g-Hf\|_2^2 + \frac{1}{2v_f}\|f\|_2^2 + \frac{1}{2v_h}\|h\|_2^2 \\ &\propto \|g-Hf\|_2^2 + \lambda_f\|f\|_2^2 + \lambda_h\|h\|_2^2, \end{aligned} \tag{10}$$

where

$$\lambda_f = \frac{v_\varepsilon}{v_f}, \quad \text{and} \quad \lambda_h = \frac{v_\varepsilon}{v_h}.$$

Observe that the regularization-based approaches using the L^2 norm fall into the Bayesian category. In regularization approaches, the cost function is chosen as the error function $\|g - Hf\|_2^2$. The regularization terms D_f and D_h are used to impose additional constraints on the optimization problem. In general, these constraints guarantee the smoothness of the image and the blur, and the effect of the smoothing terms is controlled by the regularization parameters.

2.2 The proposed method

Based on the non-blind case we performed [19], and in the situation where ε, v_ε, v_f, and v_h are known, we can use the JMAP estimation. As mentioned, this estimation is unstable and suffers from significant ringing artifacts in various applications. To overcome these limitations, we propose a regularized version using H^1 regularization terms for both f and h, by adding $D_f = \|\nabla f\|_2^2$ and $D_h = \|\nabla h\|_2^2$ to the functional (10), which gives the following energy minimization model

$$\arg\min_{(f,h)} \left\{ \|g - Hf\|_2^2 + \lambda_f \|f\|_2^2 + \lambda_1 \|\nabla f\|_2^2 + \lambda_h \|h\|_2^2 + \lambda_2 \|\nabla h\|_2^2 \right\}, \tag{11}$$

where $\nabla = (\nabla_x, \nabla_y)$ is the gradient operator combined by difference operators along horizontal and vertical directions. The last four terms are regularization terms, which ask that f and h should be smooth in H^1 sense.

The staircase effect where the smooth regions in the original image are recovered as piecewise smooth regions is partly due to the fact that the used norms are not biased against discontinuous nor continuous functions (e.g., the total variation norm (TV-norm) $:= \| \nabla u \|_1$). The functional

$$D_u = \int_\Omega |\nabla u|^2 dxdy,$$

has a strong bias against discontinuous functions [11, Page 142], so this model substantially reduces the staircase effect and recovers the smooth region's value in the image.

To discretize the gradient using a finite difference scheme, we apply the Neumann boundary condition, which is a natural option in image processing [23]. This kind of boundary condition requires that $\lambda_f \neq 0$ and $\lambda_h \neq 0$ in order to prove the coercivity of the proposed functional in the space $H^1(\Omega) \times H^1(\Omega)$, Ω is a bounded Lipschitz domain in $\mathbb{R}^2$, and then the existence of a solution of the minimization problem (11). Numerically, this alternative significantly reduces the appearance of a blurring effect in the resulting images instead of setting λ_f at 0, using an empirical reduction rule to set it from large to small, and by setting λ_h to a suitable value depending on the degradation case.

Before studying the existence of the solution for our minimization problem, an important issue is first addressed. It concerns the finiteness of image domain Ω in most practical applications. The domain Ω is often finite such as a disk or a square, in which case the blur

$$Hf = h * f(x) = \int_{\mathbb{R}^2} h(x-y) f(y) dy, \quad x \in \Omega,$$

has to be properly defined since f is only available on Ω.

There are two different ways to overcome this obstacle. First, we can modify the assumption of shift invariance of the linear operator H by allowing shift variance on Ω (H is said to be shift-invariant if for any $a \in \mathbb{R}^2, g_0(x) = H[f(x)]$ implies that $g_0(x-a) = H[f(x-a)]$). Then, the blur operator Hf remains linear, but can have a shift-variant PSF such as

$$h(x,y) = \frac{h(x-y)}{\int_\Omega h(x-z)dz}, \ \forall x,y \in \Omega,$$

for which the linear blur is updated to

$$Hf = \int_\Omega h(x,y)f(y)dy. \tag{12}$$

The second method to handle the finite domain Ω is to extrapolate f beyond Ω, rather than modifying the shift-invariant kernel within Ω as we did above. Let

$$P : f|_\Omega \longrightarrow \bar{f} = P(f)|_{\mathbb{R}^2},$$

be an appropriate linear extrapolation operator which extends f on Ω onto the entire plane (we can consider the linear operator P from $H^1(\Omega)$ to $H^1(\mathbb{R}^2)$). Then, the blur can be modified to

$$Hf(x) = h * \bar{f}(x) = h * P(f)(x) \ \ \forall x \in \Omega,$$

or equivalently, $H = \mathbb{1}_\Omega.(h * P)$, where $\mathbb{1}_\Omega(x)$ is treated as a multiplier.

More generally, suppose P is represented by some kernel $k(x,y)$ with $y \in \Omega$ and $x \in \mathbb{R}^2$. Then, the modified H is given by (12), where

$$h(x,y) = \int_{\mathbb{R}^2} h(x-z)k(z,y)dz, \ \ x,y \in \Omega.$$

For a detailed description of the above approaches, see [6].

2.2.1 The convergence behavior

We will prove the existence of the minimizer for the functional $\mathfrak{F}$ defined by

$$\begin{array}{rcl} \mathfrak{F} : H^1(\Omega) \times H^1(\Omega) & \longrightarrow & \mathbb{R} \\ (f,h) & \longmapsto & \|g - Hf\|_2^2 + \lambda_f \|f\|_2^2 + \lambda_1 \|\nabla f\|_2^2 + \lambda_h \|h\|_2^2 + \lambda_2 \|\nabla h\|_2^2 \end{array} \tag{13}$$

The proof is decomposed into three main steps

- $H^1(\Omega) \times H^1(\Omega)$ is a Hilbert space as the product of two Hilbert spaces, equipped with the norm

$$\|(f,h)\|_{H^1(\Omega)\times H^1(\Omega)} = \left(\|f\|_{H^1(\Omega)}^2 + \|h\|_{H^1(\Omega)}^2 \right)^{1/2}.$$

- $\mathfrak{F}$ is coercive on $H^1(\Omega) \times H^1(\Omega)$:

$$\begin{aligned} \mathfrak{F}(f,h) &\geq \lambda_f \|f\|_2^2 + \lambda_1 \|\nabla f\|_2^2 + \lambda_h \|h\|_2^2 + \lambda_2 \|\nabla h\|_2^2 \\ &\geq \alpha(\|f\|_2^2 + \|\nabla f\|_2^2 + \|h\|_2^2 + \|\nabla h\|_2^2) \\ &\geq \alpha(\|f\|_{H^1(\Omega)}^2 + \|h\|_{H^1(\Omega)}^2), \end{aligned} \tag{14}$$

  where $\alpha = \min(\lambda_f, \lambda_1, \lambda_h, \lambda_2) > 0$.

- $\mathfrak{F}$ is sequentially weakly lower semicontinuous.
  Let $(f_n,h_n)_n$ be a minimizing sequence. $\mathfrak{F}$ is coercive, then we can obtain a uniform bound

$$\|(f_n,h_n)\|_{H^1(\Omega)\times H^1(\Omega)} \leq C,\ C>0.$$

The space $H^1(\Omega)\times H^1(\Omega)$ is reflexive, then by weak sequential compactness theorem (see [2]) we can deduce the existence of $(\tilde{f},\tilde{h}) \in H^1(\Omega)\times H^1(\Omega)$ and of a subsequence denoted also by $(f_n,h_n)_n$ such that

$$(f_n,h_n) \overset{H^1(\Omega)\times H^1(\Omega)}{\searrow} (\tilde{f},\tilde{h}).$$

The subsequence $(f_n,h_n)_n$ is bounded in $H^1(\Omega)\times H^1(\Omega)$ and since the embedding $H^1(\Omega) \hookrightarrow L^2(\Omega)$ is compact, then $(f_n,h_n)_n$ has a subsequence (still denoted by $(f_n,h_n)_n$) convergent in $L^2(\Omega)$, we get finally

$$\begin{cases} f_n \overset{H^1(\Omega)}{\searrow} \tilde{f} \\ h_n \overset{H^1(\Omega)}{\searrow} \tilde{h} \end{cases} \quad \text{and} \quad \begin{cases} f_n \overset{L^2(\Omega)}{\longrightarrow} \tilde{f} \\ h_n \overset{L^2(\Omega)}{\longrightarrow} \tilde{h} \end{cases} \tag{15}$$

As the convergence in L^2 implies L^2 norm convergence, we obtain

$$\begin{cases} \|f_n\|_2^2 \longrightarrow \|\tilde{f}\|_2^2 \\ \|h_n\|_2^2 \longrightarrow \|\tilde{h}\|_2^2 \end{cases} \tag{16}$$

From the weakly convergent sequence $(f_n,h_n)_n$ in $H^1(\Omega)\times H^1(\Omega)$ and the weak continuity of operator $\nabla : H^1(\Omega) \to L^2(\Omega)$, we get

$$\begin{cases} \nabla f_n \overset{L^2(\Omega)}{\searrow} \nabla\tilde{f} \\ \nabla h_n \overset{L^2(\Omega)}{\searrow} \nabla\tilde{h} \end{cases} \tag{17}$$

which implies that

$$\begin{cases} \liminf_{n\to+\infty} \|\nabla f_n\|_2^2 \geq \|\nabla\tilde{f}\|_2^2 \\ \liminf_{n\to+\infty} \|\nabla h_n\|_2^2 \geq \|\nabla\tilde{h}\|_2^2 \end{cases} \tag{18}$$

For the fidelity term, we have

$$\begin{aligned} \left|\int_\Omega (h_n * f_n - g)^2 - \int_\Omega (\tilde{h} * \tilde{f} - g)^2\right| &= \left|\int_\Omega (h_n * f_n - g - \tilde{h} * \tilde{f} + g)(h_n * f_n - g + \tilde{h} * \tilde{f} - g)\right| \\ &\leq \|h_n * f_n - \tilde{h} * \tilde{f}\|_2 \|h_n * f_n + \tilde{h} * \tilde{f} - 2g\|_2 \\ &\leq \|h_n * (f_n - \tilde{f}) + (h_n - \tilde{h}) * \tilde{f}\|_2 \left(\|h_n\|_1\|f_n\|_2 + \|\tilde{h}\|_1\|\tilde{f}\|_2 + 2\|g\|_2\right) \\ &\leq \left(\|h_n\|_1\|f_n - \tilde{f}\|_2 + \|h_n - \tilde{h}\|_2\|\tilde{f}\|_1\right)\left(\|h_n\|_1\|f_n\|_2 + \|\tilde{h}\|_1\|\tilde{f}\|_2 + 2\|g\|_2\right). \end{aligned}$$

As $\|f_n\|_{H^1(\Omega)} \leq C$ (respectively $\|h_n\|_{H^1(\Omega)} \leq C$), then

$$\|f_n\|_{L^2(\Omega)} \leq C \ \ (\text{respectively} \|h_n\|_{L^2(\Omega)} \leq C).$$

Using the Sobolev injection $L^2(\Omega) \hookrightarrow L^1(\Omega)$, we have

$$\|h_n\|_{L^1(\Omega)} \leq K.$$

Finally, we obtain

$$\|h_n * f_n - g\|_2^2 \longrightarrow \|\tilde{h} * \tilde{f} - g\|_2^2.$$

Then, according to the following theorem (see [2, Page 91])

Theorem 1 (Existence)**.** *Let E be a reflexive Banach space and $\mathfrak{F} : E \longrightarrow \mathbb{R}$ is a sequentially weakly lower semicontinuous and coercive function, then the problem* $\inf_{u\in E} \mathfrak{F}(u)$ *has a solution. Furthermore, if $\mathfrak{F}$ is strictly convex, then this solution is unique.*

$(\tilde{f}, \tilde{h})$ is a minimizer of functional $\mathfrak{F}$ in the space $H^1(\Omega) \times H^1(\Omega)$. Unfortunately, this solution is not unique. If, for example, (f,h) is a solution of (11), then $(-f,-h)$ is also a solution.

2.2.2 Alternating minimization algorithm

In the Fourier domain, our model (11) is equal to

$$\underset{(\mathscr{F},\mathscr{H})}{\arg\min} \left\{ \|\mathscr{G} - \mathscr{H}\mathscr{F}\|_2^2 + \lambda_f \|\mathscr{F}\|_2^2 + \lambda_1 \|D\mathscr{F}\|_2^2 + \lambda_h \|\mathscr{H}\|_2^2 + \lambda_2 \|D\mathscr{H}\|_2^2 \right\}, \tag{19}$$

where $\mathscr{F}$, $\mathscr{H}$, $\mathscr{G}$, and $D = (D_x, D_y)$ are the Fourier transforms of f, h, g, and $\nabla = (\nabla_x, \nabla_y)$, respectively, and we have

$$\|D\mathscr{U}\|_2^2 = \|D_x\mathscr{U}\|_2^2 + \|D_y\mathscr{U}\|_2^2. \tag{20}$$

By taking the Wirtinger derivative of functional in (19) with respect to $\mathscr{H}$ and $\mathscr{F}$ respectively, and setting the result to be zero, we get the Euler-Lagrange equations

$$\begin{cases} -\overline{\mathscr{F}}\mathscr{G} + |\mathscr{F}|^2\mathscr{H} + \lambda_h\mathscr{H} + \lambda_2|D|^2\mathscr{H} = 0 \\ -\overline{\mathscr{H}}\mathscr{G} + |\mathscr{H}|^2\mathscr{F} + \lambda_f\mathscr{F} + \lambda_1|D|^2\mathscr{F} = 0 \end{cases} \tag{21}$$

where $|D|^2 = |D_x|^2 + |D_y|^2$.

When $\mathscr{F}$ is given, we can obtain the optimized expression for $\mathscr{H}$:

$$\tilde{\mathscr{H}} = \frac{\overline{\mathscr{F}}\mathscr{G}}{|\mathscr{F}|^2 + \lambda_h + \lambda_2|D|^2}. \tag{22}$$

Then, we can obtain $\mathscr{F}$ using the previous $\mathscr{H}$:

$$\tilde{\mathscr{F}} = \frac{\overline{\mathscr{H}}\mathscr{G}}{|\mathscr{H}|^2 + \lambda_f + \lambda_1|D|^2}. \tag{23}$$

We use inverse Fourier transforms to get the estimations.

Algorithm 1 Blind MAP-H^1 algorithm in Fourier domain

1: Compute the regularization operator $D = (D_x, D_y)$.
2: **Initialization**: $f = g$, $h = \delta$ the Dirac function, λ_f, λ_h, r, $\lambda_f^{\min}$.
3: **repeat** Optimizing h and f
4: Calculate λ_1 and λ_2 using the subproblems of $\mathscr{F}$ and $\mathscr{H}$ respectively, and the GCV function obtained in our paper [19].
5: Update $\mathscr{H}$ defined in (22).
6: Find the inverse Fourier transform of $\mathscr{H}$.
7: Impose the kernel constraint using projection on the convex set: $C_1 := \{h \,/\, h \geq 0, \sum_n h(n) = 1\}$.
8: Update $\mathscr{F}$ using $\mathscr{H}$ in the previous step with the help of (23).
9: Find the inverse Fourier transform of $\mathscr{F}$.
10: Impose the image constraint using projection on the convex set: $C_2 := \{f \,/\, 0 \leq f(n) \leq 1, \forall n\}$.
11: Set λ_f from large to small according to the empirical reduction rule: $\lambda_f^{t+1} = \max\left(\lambda_f^t . r, \lambda_f^{\min}\right)$.
12: **end** Iterations have been performed
13: **Output**: $\tilde{f}$, $\tilde{h}$

3 Results and discussion

In the present section, we give experimental results of the proposed algorithm and compare it with the popular state-of-the-art blind image deconvolution methods, including the blind Richardson-Lucy algorithm and the iterative Wiener filter method.

Note that, our algorithm is not sensitive to the initial guess of the image and the kernel we used. Furthermore, as it is well known, the stopping criteria play a major role in iterative algorithms. However, in our case, it was not easy to find good criteria for our test data. Therefore, based on interactive monitoring of the iterative processes, we stop the iteration when the change in the reconstruction obtained from an iteration step was no longer observable.
Any algorithm that implements deconvolution in Fourier domain should do something to avoid ringing artifacts at the image boundaries. We add black boundaries with 50 pixels on each side of the test images in all experiments, and we process the image near the boundaries using the MATLAB *edgetaper* command in the iterative Wiener filter algorithm.
Generally, the Richardson-Lucy algorithm takes considerable computation to obtain a stable solution. In the blind case, it becomes a very challenging problem, and we consider the number of iterations as the stopping criterion.

We use five images in our tests, which are the standards for image processing (Figure 1). The degraded versions are obtained by convolving these original images with the following blur kernels:

- Binary blur kernel of size 21×21 with normalized elements to sum 1 (Figure 2).
- Gaussian blur kernel of size 20×20 with standard deviation 3 (fspecial('gaussian', 20, 3)).
- Motion blur kernel of length 15 (fspecial('motion', 15)).

Figure 1: Set of five images used in the tests. This is a set of five images used as an original image in the tests.

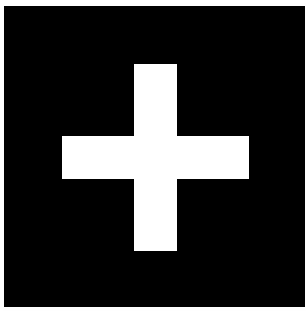

Figure 2: First kernel of convolution. The first kernel used to blur images.

The quality of the reconstructions evaluated using two criteria: the peak signal to noise ratio (PSNR) given below:

$$PSNR(\tilde{f},f) = 10\log 10(\frac{255^2}{\frac{1}{st} \parallel \tilde{f}-f \parallel_2^2}),$$

where s and t are numbers of row and column of the image. The second criterion is the structural similarity index measure (SSIM), which is an image quality metric that assesses the visual impact of

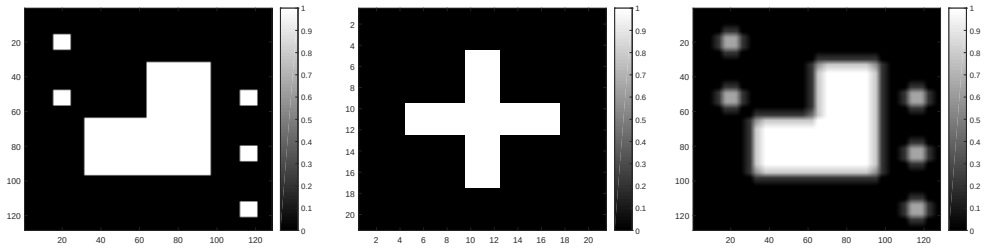

(a) (b) (c) PSNR = 17.93 SSIM = 0.7270

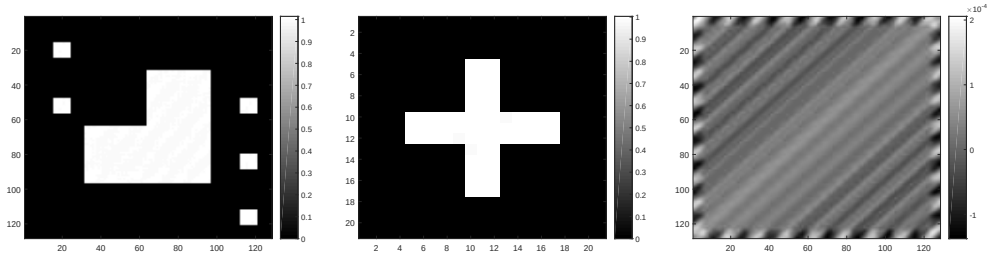

(d) PSNR = 49.93 SSIM = 0.9788 (e) MSE = 4.11×10^{-09} (f)

Figure 3: Test on a synthetic image degraded by kernel 2. (a) Original image; (b) kernel of convolution; (c) degraded image; (d) and (e) are restored image and estimated kernel, respectively, using our approach; (f) the error plot using (c) and the degraded image obtained from (d) and (e).

three characteristics of an image: luminance, contrast, and structure. Both metrics are popular standard image quality measures that are quite used in comparing image restoration results.

We show the blind image deconvolution reconstructions of the first test we performed (Figure 3), which illustrate the effectiveness of our approach in both image restoration and kernel estimation. Visually, we have obtained a restored image (d) and an estimated kernel (e) that are very close to the true ones: (a) and (b). For quantitative comparison, we were able to produce a sharp image with a PSNR that exceeds twice the initial value and a remarkable SSIM much greater than the first one. We calculated also the mean squared error (MSE$(\tilde{h},h) = \mathbb{E}(\|\tilde{h}-h\|_2^2)$), which is a standard measure for estimating errors of kernels when they are normalized and have the same size. It is obvious that the MSE of the proposed approach is much smaller, which implies that our algorithm gives a better estimation of the blur kernel too. The error plot (f) that uses the degraded image (c) and the degraded image obtained from (d) and (e) confirms these results. It is clear that our method succeeds to restore the finer details in the image. For the remaining tests, we present the results in Figures 4, 5, 6, 7, and 8, and PSNR and SSIM values in Tables 1, 2, and 3. In all these cases, we have found that our technique can successfully deblur the most degraded images compared with the iterative Wiener filter method and the blind Richardson-Lucy algorithm. We can observe that the restored images using these two approaches are still somewhat blurry and the ringing artifacts are obvious here. The proposed model gives better deblurring results as the edges are sharper and the ringing artifacts are negligible. Several close-ups in the figures also illustrate the high

quality achieved in the reconstruction using our approach: oversmoothing is strongly reduced and small details are recovered. In terms of image quality measures, the proposed blind MAP$-H^1$ model has the highest PSNR and SSIM values among all, the blind Richardson-Lucy algorithm is the second-best, in general, followed by the iterative Wiener filter method.

Table 1: PSNR and SSIM values obtained by three methods for five different images degraded by kernel 1. For each test setting, four results are provided: Blurred, blind Richardson-Lucy (RL) algorithm, iterative Wiener filter (IWF) method, and our proposed blind MAP-H^1 model. *Bold* format: the best score in each line.

Image	Size	Measure	Blurred	Method		
				Blind RL	IWF	Blind MAP-H^1
Cameraman	512×512	PSNR	24.66	28.83	28.49	**30.67**
		SSIM	0.7824	0.6639	0.6380	**0.8570**
House	256×256	PSNR	25.09	29.36	29.89	**31.48**
		SSIM	0.7379	0.8018	0.7576	**0.8774**
Couple	512×512	PSNR	24.17	29.38	30.48	**31.62**
		SSIM	0.6127	0.8401	0.8734	**0.9029**
Pirate	512×512	PSNR	24.75	29.78	29.74	**31.49**
		SSIM	0.6268	0.8367	0.7847	**0.8751**
Boat	512×512	PSNR	23.98	29.25	30.36	**30.63**
		SSIM	0.6181	0.8264	0.8603	**0.8726**

Table 2: PSNR and SSIM values obtained by three methods for five different images degraded by kernel 2. For each test setting, four results are provided: Blurred, blind Richardson-Lucy (RL) algorithm, iterative Wiener filter (IWF) method, and our proposed blind MAP-H^1 model. *Bold* format: the best score in each line.

Image	Size	Measure	Blurred	Method		
				Blind RL	IWF	Blind MAP-H^1
Cameraman	512×512	PSNR	24.38	28.88	29.05	**30.12**
		SSIM	0.7737	0.8567	0.8687	**0.8844**
House	256×256	PSNR	24.74	27.69	27.88	**29.10**
		SSIM	0.7264	0.7510	0.7702	**0.7821**
Couple	512×512	PSNR	23.60	26.13	26.58	**26.82**
		SSIM	0.5625	0.6928	0.7200	**0.7334**
Pirate	512×512	PSNR	24.67	27.37	27.17	**28.27**
		SSIM	0.6282	0.7392	0.7338	**0.7830**
Boat	512×512	PSNR	23.63	27.03	26.94	**27.49**
		SSIM	0.5939	0.7427	0.7418	**0.7648**

Table 3: PSNR and SSIM values obtained by three methods for five different images degraded by kernel 3. For each test setting, four results are provided: Blurred, blind Richardson-Lucy (RL) algorithm, iterative Wiener filter (IWF) method, and our proposed blind MAP-H^1 model. *Bold* format: the best score in each line.

Image	Size	Measure	Blurred	Method		
				Blind RL	IWF	Blind MAP-H^1
Cameraman	512×512	PSNR	23.12	28.09	29.07	**32.21**
		SSIM	0.7821	0.8891	0.8190	**0.9015**
House	256×256	PSNR	24.79	28.68	27.89	**30.50**
		SSIM	0.7639	0.8470	**0.8575**	0.8325
Couple	512×512	PSNR	23.68	26.77	25.64	**28.30**
		SSIM	0.6191	0.7796	0.7649	**0.8183**
Pirate	512×512	PSNR	24.04	30.04	29.99	**30.91**
		SSIM	0.6217	0.8511	0.8598	**0.8811**
Boat	512×512	PSNR	23.32	28.41	28.35	**29.73**
		SSIM	0.6408	0.8306	0.8333	**0.8608**

4 Conclusions

In this paper, we have considered the blind image deconvolution problem. We have extended the supervised Bayesian approach by adding H^1 regularization terms on both the sharp image and the blur kernel, and by proposing useful techniques to deal with the estimation of smoothing parameters. An existence result for our model was given. The proposed algorithm is simple, easy to implement, and gives quite satisfactory results compared to some available methods, which gives confidence in the efficiency of our model.

Acknowledgements

We would like to thank the anonymous referee for all the valuable remarks and useful suggestions that helped us to improve the quality of the paper.

References

[1] H.C. Andrews, B.R. Hunt, *Digital Image Restoration*, New Jersey: Prentice-Hall, 1977.

[2] H. Attouch, G. Buttazzo, G. Michaille, *Variational Analysis in Sobolev and BV Spaces: Applications to PDEs and Optimization*, Philadelphia: SIAM, 2014.

[3] G.R. Ayers, J.C. Dainty, *Iterative blind deconvolution method and its applications*, Opt. Lett. **13** (1988) 547–549.

[4] R.H.T. Bates, *Astronomical speckle imaging*, Phys. Rep. **90** (1982) 203–97.

Figure 4: Deconvolution of *Cameraman* image. From left to right, the first column represents degradation by kernel 1, the second column for the degradation by kernel 2, and by kernel 3 in the third column. From top to bottom, the order of the rows is as follows: blurred images using the three kernels respectively, restored images using blind Richardson-Lucy algorithm [12], restored images using iterative Wiener filter method [3], and finally the restored images using our proposed blind MAP-H^1 model.

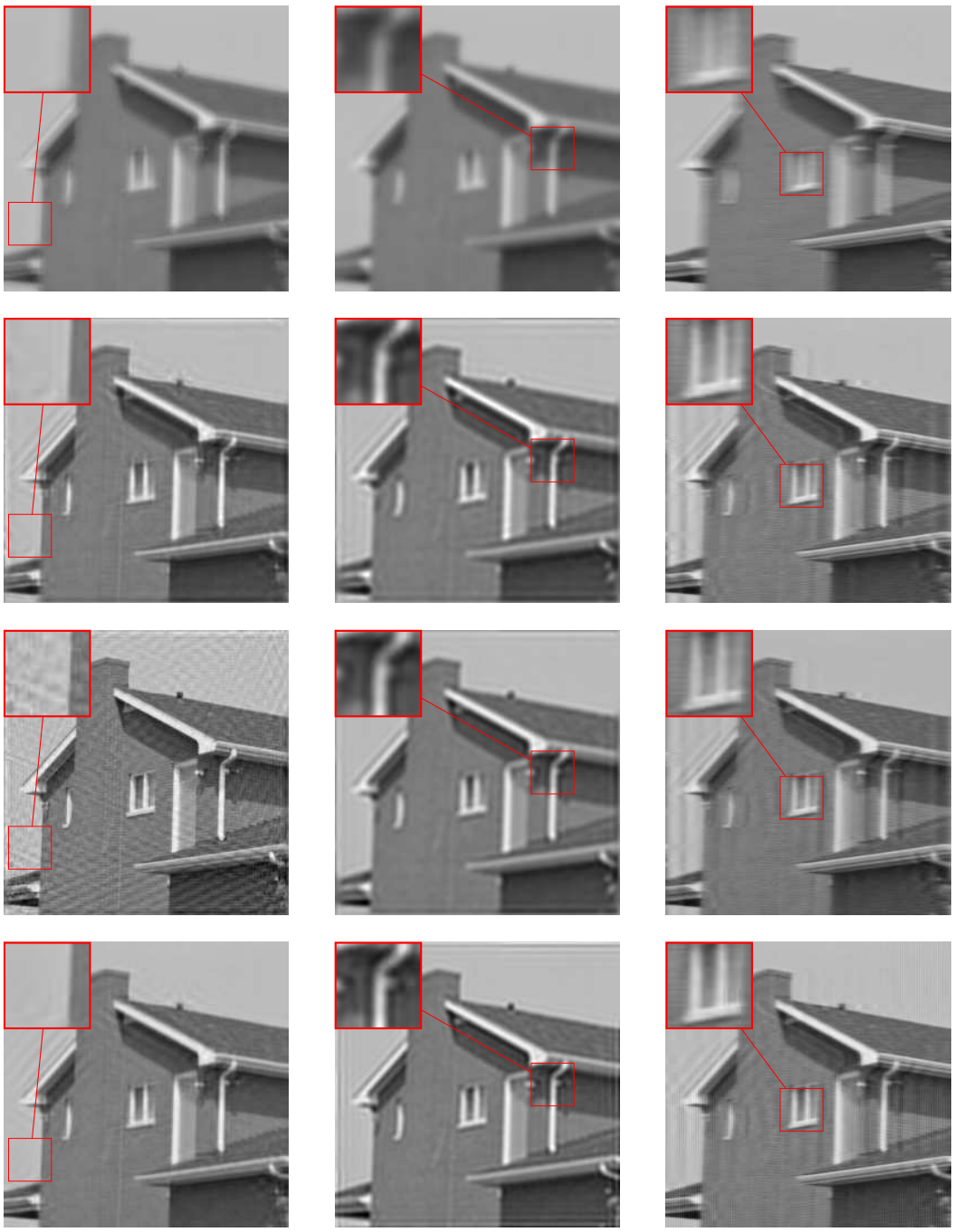

Figure 5: Deconvolution of *House* image. From left to right, the first column represents degradation by kernel 1, the second column for the degradation by kernel 2, and by kernel 3 in the third column. From top to bottom, the order of the rows is as follows: blurred images using the three kernels respectively, restored images using blind Richardson-Lucy algorithm [12], restored images using iterative Wiener filter method [3], and finally the restored images using our proposed blind MAP-H^1 model.

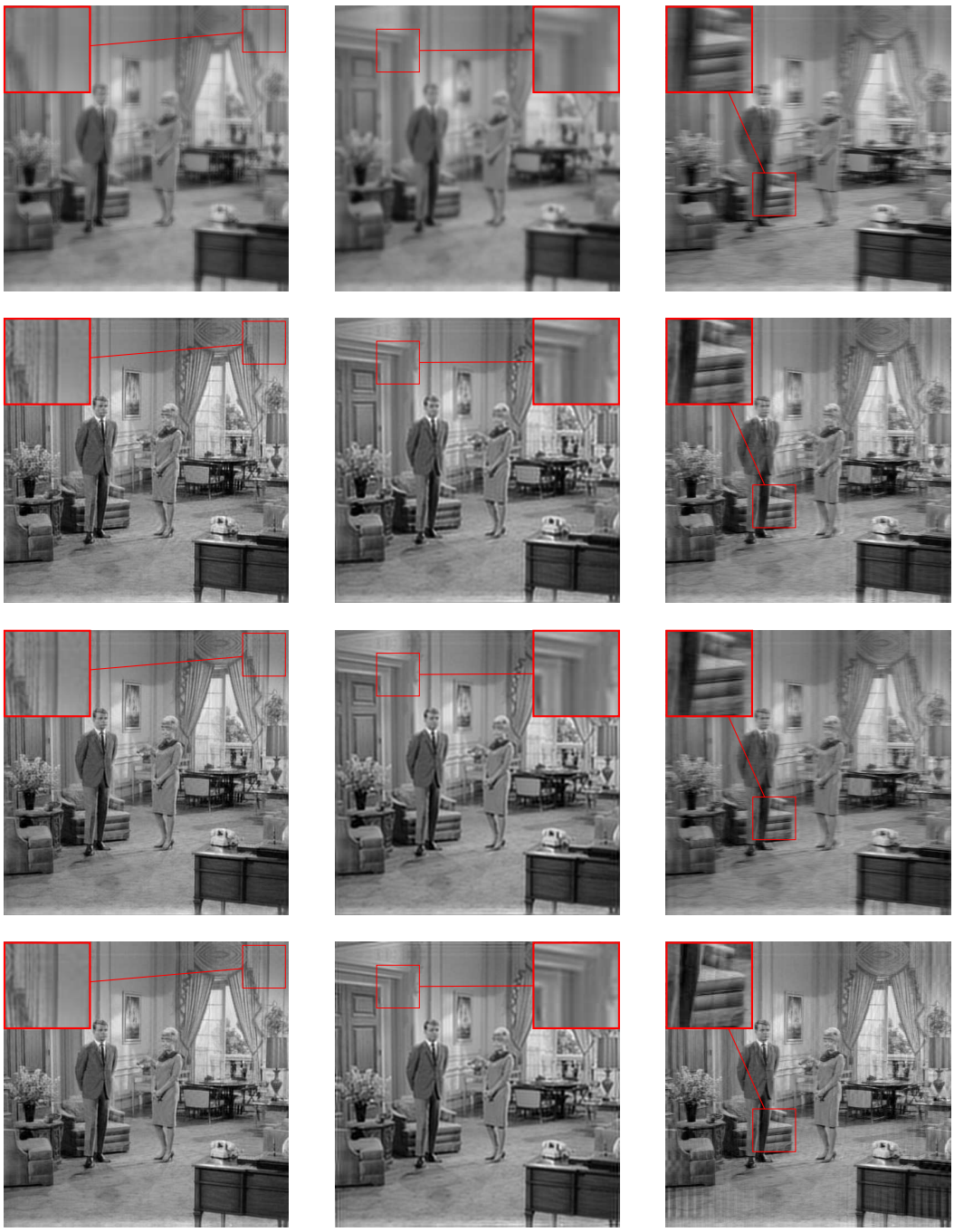

Figure 6: Deconvolution of *Couple* image. From left to right, the first column represents degradation by kernel 1, the second column for the degradation by kernel 2, and by kernel 3 in the third column. From top to bottom, the order of the rows is as follows: blurred images using the three kernels respectively, restored images using blind Richardson-Lucy algorithm [12], restored images using iterative Wiener filter method [3], and finally the restored images using our proposed blind MAP-H^1 model.

Figure 7: Deconvolution of *Pirate* image. From left to right, the first column represents degradation by kernel 1, the second column for the degradation by kernel 2, and by kernel 3 in the third column. From top to bottom, the order of the rows is as follows: blurred images using the three kernels respectively, restored images using blind Richardson-Lucy algorithm [12], restored images using iterative Wiener filter method [3], and finally the restored images using our proposed blind MAP-H^1 model.

Figure 8: Deconvolution of *Boat* image. From left to right, the first column represents degradation by kernel 1, the second column for the degradation by kernel 2, and by kernel 3 in the third column. From top to bottom, the order of the rows is as follows: blurred images using the three kernels respectively, restored images using blind Richardson-Lucy algorithm [12], restored images using iterative Wiener filter method [3], and finally the restored images using our proposed blind MAP-H^1 model.

[5] J. Biemond, R.L. Lagendijk, R.M. Mersereau, *Iterative methods for image deblurring*, Proc. IEEE. **78** (1990) 856–883.

[6] T.F. Chan, J. Shen, *Image Processing and Analysis: Variational, PDE, Wavelet, and Stochastic Methods*, Philadelphia: SIAM, 2005.

[7] M.J.B. Crowther, M.C. Fernandez, *Imaging in videoconferencing now: telemedicine in Somalia*, Adv. Imaging. **8** (1993) 28–31.

[8] S.N. Drossos, *Fast artifact free reconstruction algorithm for limited data (PET) using constrained optimization*, Third Int. Conf. on Image Processing and its Applications, Warwick, UK, (1989) 367–372.

[9] I. El Mourabit, *Quelques problèmes variationnels et EDP appliqués au traitement de l'image*, Ph.D. Thesis, FSTG, Cadi Ayyad University, Morocco, 2017.

[10] K. Faulkner, C.J. Kotre, M. Louka, *Veiling glare deconvolution of images produced by x-ray image intensifiers*, Third Int. Conf. on Image Processing and its Applications, Coventry, UK, (1989) 669–673.

[11] N.M.F. Ferreira, J.A.T. Machado, *Mathematical Methods in Engineering*, Springer Netherlands; 2014.

[12] D.A. Fish, A.M. Brinicombe, E.R. Pike, J. G. Walker, *Blind deconvolution by means of the Richardson-Lucy algorithm*, JOSA A. **12** (1995) 58–65.

[13] P.C. Hansen, *Regularization tools: a Matlab package for analysis and solution of discrete ill-posed problems*, Numer. Algorithms **6** (1994) 1–35.

[14] A. Jain, S. Ranganath, *Application of two dimensional spectral estimation in image restoration*, IEEE Int. Conf. on Acoustics, Speech, and Signal Processing (ICASSP'81), Atlanta, Georgia, USA, **6** (1981) 1113–1116.

[15] A.K. Katsaggelos, *Digital Image Restoration*, Berlin Heidelberg: Springer-Verlag, 1991.

[16] V. Krishnamurthi, Y.H. Liu, T.J. Holmes, B. Roysam, J.N. Turner, *Blind deconvolution of 2D and 3D fluorescent micrographs*, Biomedical Image Processing and Three-Dimensional Microscopy, San Jose, CA, United States, **1660** (1992) 95–102.

[17] D. Kundur, D. Hatzinakos, *A novel recursive filtering method for blind image restoration*, IASTED Int. Conf. on Signal and Image Processing, Las Vegas, NV, USA, (1995) 428–431.

[18] D. Kundur, D. Hatzinakos, *A novel blind deconvolution scheme for image restoration using recursive filtering*, IEEE Trans. Signal Process. **46** (1998) 375–390.

[19] B. Laaziri, S. Raghay, A. Hakim, *Regularized supervised Bayesian approach for image deconvolution with regularization parameter estimation*, EURASIP J. Adv. Signal Process. **2020** (2020) 1–16.

[20] F. Li, X.G. Lv, Z. Deng, *Regularized iterative Weiner filter method for blind image deconvolution*, J. Comput. Appl. Math. **336** (2018) 425–438.

[21] A. Mohammad-Djafari, *Inverse problems in imaging systems and the general Bayesian inversion framework*, J. Iran. Assoc. Electr. Electron. Eng. **3** (2006) 3–21.

[22] J.P. Muller, *Digital Image Processing in Remote Sensing*, Philadelphia: Taylor & Francis, 1988.

[23] M.K. Ng, R.H. Chan, W.C. Tang, *A fast algorithm for deblurring models with Neumann boundary conditions*, SIAM J. Sci. Comput. **21** (1999) 851–866.

[24] P. Nisenson, R. Barakat, *Partial atmospheric correction with adaptive optics*, JOSA A. **4** (1987) 2249–2253.

[25] A.G. Qureshi, H.T. Mouftah, *Partially-blind image restoration using constrained Kalman filtering*, IEEE Int. Conf. on Acoustics, Speech, and Signal Processing (ICASSP 91), Toronto, Ontario, Canada, (1991) 3713–3714.

[26] M.C. Roggemann, *Limited degree-of-freedom adaptive optics and image reconstruction*, Appl. Opt. **30** (1991) 4227–4233.

[27] T.J. Schulz, *Multiframe blind deconvolution of astronomical images*, JOSA A. **10** (1993) 1064–1073.

[28] R. Wang, D. Tao, *Recent progress in image deblurring*, arXiv preprint, 2014, https://arxiv.org/abs/1409.6838.

[29] T. Wilson, S.J. Hewlett, *Imaging strategies in three-dimensional confocal microscopy*, Proc. SPIE Biomedical Image Processing, San Jose, California, USA, **1245** (1991) 35–45.